Physical properties of PVDF-GO/black-TiO$_2$ nanofibers and its photocatalytic degradation of methylene blue and malachite green dyes

Muhammed Abdelmaksoud[1,2] · Alaa Mohamed[3,4] · Abderrahman Sayed[1,2] · Sherif Khairy[1]

Abstract

Black TiO$_2$ and graphene oxide (GO) have attracted intensive attention as an effective catalyst on visible light driven for photodegrading of dyes. In this study, nano-black TiO$_2$ was prepared by a simple hydrogenation of the anatase titanium oxide, and the graphene oxide was prepared by applying the modified Hummers method. The diffuse reflectance spectroscopy has been investigated to find out the optical energy gaps of the treated and nano-black samples. The prepared powders and nanofiber membranes are carefully examined to ensure their single phase and compound structure formation as well as to measure the equivalent crystallite size and particle distributions. The optimum degradation efficiency of malachite green and methylene blue dyes occurred at pH values of 8 and 10, respectively. The maximum photocatalytic degradation efficiencies of malachite green (MG) and methylene blue (MB) were found to be 74 and 39%, respectively, under visible light after 30 min. The degradation efficiency of MG is peaked at pH 8 and 20 mg of the nano-black TiO$_2$. The stability and flexibility of the nanofibers allow their application in a continuous system and can be reused after several cycles.

Introduction

Industrial wastewaters, especially from textile, pharmaceutical, cosmetic, pulp and paper, and processing industries, usually contain large amounts of dye contaminants (Khalil, Aboamera et al. 2019, Zhang et al. 2019). As many dyes are toxic and even carcinogenic, the discharge of dye containing wastewaters to the environment certainly poses a serious threat to the environment (Karim et al. 2019). Titanium dioxide (TiO$_2$) nanoparticle has been extensively investigated for numerous applications, for example, a white pigment (El-Sherbiny et al. 2014), UV absorber in sunscreens (Smijs and Pavel 2011), photocatalyst for hydrogen generation (Mapukata et al. 2020), environmental pollution removal (Salama et al. 2018; Abdel-Mottaleb et al. 2019a, b), and photo-electrochemical sensors (Zhong et al. 2019; Mendonça et al. 2020). Moreover, it is considered one of the well-known catalyst as a consequence of its availability, low-cost, non-toxicity, and relatively high chemical stability (Yazdi et al. 2018; Khalil et al. 2019a, b). It exists in three crystalline phases, namely, tetragonal anatase, tetragonal rutile, and orthorhombic brookite (Park and Kim 2005). As a result of their higher photoactivity, both of the two phases, rutile and anatase have been widely used (Chalastara et al. 2020). Nevertheless, they absorb only the UV light, since their band gap energies are somewhat wide, 3.2 and 3.0 eV for anatase and rutile phases respectively (Batzill et al. 2006). Besides, TiO$_2$ shows a low quantum efficiency since the photogenerated electron-hole

Responsible Editor: Sami Rtimi

✉ Alaa Mohamed
alakha@kth.se

[1] Physics Department, Faculty of Science, Cairo University, Giza, Egypt

[2] Faculty of Nanotechnology for Postgraduate Studies, Cairo University, El Sheikh Zayed 12588, Egypt

[3] Department of Mechatronics, Canadian International College, Fifth Settlement, New Cairo, Egypt

[4] Institute of Functional Interfaces (IFG), Karlsruhe Institute of Technology (KIT), Hermann von Helmholtz Platz 1, 76344 Eggenstein Leopoldshafen, Germany

pairs are rapidly recombined (Bai and Zhou 2014). Therefore, to improve the photocatalytic activity of TiO_2, it is essential to improve its optical absorption range and charge separation. Black titanium dioxide (TiO_2) with low value of band gap (1.54 eV) has been one of the most researched photocatalyst in recent years. Its ability to overcome the limitations of pristine TiO_2 through enhanced visible light absorption and reduced recombination of photogenerated charge carriers has gathered the attention of the scientific community since its discovery in 2011 (Chen et al. 2011; Rajaraman et al. 2020). Moreover, the structural, chemical, electronic, and optical properties of TiO_2 nanoparticles have been radically changed through hydrogenation. Furthermore, graphene oxide (GO) has a low band gap and high conductivity properties which improve the catalytic properties (Abdel-Mottaleb et al. 2019a, b; Aboamera et al. 2019).

Large-scale processing and the widespread use of synthetic dyes cause significant contamination to the atmosphere (Yazdi et al. 2018). Dyes are used in both commercial and analytical fields and are biologically and chemically difficult to decompose (Aboamera et al. 2018). It is applied as a histological dye, an antifungal drug, a carcinogenic agent, a teratogenic agent, an environmental contaminant, and an antibacterial agent, causing extreme effects in water bodies because it decreases light penetration and thus leading to a demise of aquatic life (Sudova et al. 2007; Karim et al. 2018). These dyes escape from traditional water treatment processes and stay in the environment. Nanofibers with controllable structural characteristics such as diameter, pore size, and pore ratio were manufactured by adjusting the processing parameters in the electrospinning technique (Mohamed 2019; Mohamed et al. 2019b). Poly(vinylidene fluoride) (PVDF) is a polymer with desirable behaviors including high mechanical, chemical, and thermal stability properties. Different processing methods of PVDF lead to five crystalline polymorph phases (Salimi and Yousefi 2003). Two of these polymers are non-polar, whereas the other three are polar and demonstrate ferroelectric and piezoelectric properties (Castkova et al. 2020). α, β, and γ phases are the most frequently explored as a result of their properties and widespread applications (Ruan et al. 2018). This work investigates the synthesis of black-TiO_2, GO, electrospun of PVDF-GO nanofiber, and PVDF-GO/black-TiO_2 composite nanofiber membrane for the photocatalytic degradation of malachite green (MG) and methylene blue (MB) under visible light. The effect of various parameters such as pH, initial dye concentration, contact time, and catalyst dose was evaluated. Nanofibers are recyclable which makes this technique in wastewater treatment cheap and green.

Experimental

Materials

Titanium dioxide (TiO_2, Anatase powder 98%), sodium hydroxide pellets (NaOH, 98%), and sodium borohydride (NaBH4, 95%) were from ADVENT CHEMBIO PVT., LTD.; sodium chloride (NaCL, 98.5%) was from Egyptian Salt and Minerals Co.; graphite powder (particle size 150 mesh 90% min) was from Nice Chemicals Ltd.; sulfuric acid (H_2SO_4, 98%) was from S D Fine Chem Ltd.; potassium permanganate ($KMnO_4$, 98%) was from El Goumhouria, Egypt; hydrogen peroxide (H_2O_2, 30%) was from PioChem for laboratory chemicals; hydrochloric acid (HCl, 37%) was from Honeywell Specialty Chemicals Seelze, Germany; acetone (2-propanon, 99.5%) was from Diachem; *N*,*N*-dimethyl formamide (DMF, 99%) was from Alfa Aesar; poly(vinylidene fluoride) (PVDF) pellets ($M_w = 275,000$) was from Sigma-Aldrich; glutaraldehyde (GA, 50%) was from Fine Chemicals; ethyl alcohol (ethanol, 99%) was from PioChem for laboratory chemicals; malachite green (MG) was from Sigma-Aldrich; and methylene blue (MB) was from the Science Lab.

Preparation of treated TiO_2 nanoparticles

A total of 2.5 g of anatase TiO_2 bulk powder was dissolved into 150 mL NaOH solution (10 M) at room temperature, applying vigorous stirring for 2 h. Then, the solution was placed in ambient temperature for 2 h in an ultrasonic bath (Sonica 4200, 40 kHz and 800 W). The precipitates were centrifuged then washed with deionized water until the solution is neutralized. Afterward, the precipitates were dried at 120 °C (Arami et al. 2007).

Preparation of nano-black TiO_2

TiO_2 and $NaBH_4$ with a respective molar ratio of 1:2 were mixed. Specifically, 0.7987 g of anatase TiO_2 and 0.7566 g of $NaBH_4$ were mixed thoroughly; then the mixture was grinded for 15 min to homogenize it. Afterwards, a small stainless autoclave was used to heat the mixture up to 325 °C for 16 h. As a substitute of the vacuum system with Ar atmosphere, the mixture was perfectly fit in between a double layer of NaCl powder to make sure that the mixture is chemically isolated. Finally, the black TiO_2 was dried at 120 °C, after being washed repeatedly with distilled water to neutralize the solution.

Preparation of graphene oxide

An excessive oxidation technique of graphite by adding $KMnO_4$ and H_2SO_4 has been utilized to synthesize GO which

is known as the modified Hummers method. Explicitly, graphite powder (2 g) was stirred in 98% H_2SO_4 (45 mL) for 1 h. Then 6 g of $KMnO_4$ was gradually added to the above solution while keeping the temperature at less than 20 °C through an ice bath. After the temperature has been stabilized, the solution was kept stirring at room temperature for another 1.5 h. The solution was put back into the ice bath and diluted through the addition of 90 mL of distilled water, keeping a forceful stirring. Furthermore, 30% H_2O_2 solution (10 mL) and distilled water (150 mL) were added while maintaining the stirring. Repeated centrifugation was employed to wash the graphene oxide (GO), mainly with 5% HCl aqueous solution followed by distilled water until the solution pH became neutral. GO was then dried under 60 °C to prevent changing to reduced graphene oxide (RGO).

Preparation of PVDF-GO nanofiber

The electrospinning method has been applied to synthesize PVDF-GO nanofiber membranes. The applicable solution with 20 wt% of PVDF pellets and 0.3 wt% of GO were mixed together into a DMF/acetone (v/v 3/2) solvent, and the resulting solution was placed into a sonicator for 15 min. Then, the prepared solution was stirred at a temperature lower than 60 °C for 2 h to obtain a homogeneous solution. The solution was then filled into a 5-mL syringe with a 22-gauge needle. The syringe was positioned vertically for a minute, and the air was completely removed by pushing the end of the syringe plunger. The flow rate was controlled by NE-300 (New Era Pump System Inc.) and the voltage supply equipment used was a 73,030 N (Genvolt General High Voltage Ind., Ltd.). The following conditions were employed: a flow rate of 1 mL/h, a voltage of 23.5 kV, and a TCD (tip to collector distance) of 15 cm. As a last step, the membrane was left to dry at room temperature.

Preparation of PVDF-GO/NB-TiO$_2$ composite nanofibers

An area of 3× 3 cm^2 PVDF-GO composite nanofiber was submerged into the crosslinking medium with 2.5 wt.% glutaraldehyde (GA) and was kept soaking at room temperature for 20 h. The NB NPs quantity (5, 10, and 20 mg) was then added to 7 mL of distilled water, and the solution was placed into an ultrasonic bath for 15 min. After the membrane was dried, the ultrasonicated solution was added to the composite nanofiber into a 4-cm diameter petri dish, which was kept shaking in an orbital shaker SO1 (Stuart Scientific) for 17 h. The cross-linked composite nanofibers were dried, then washed out with deionized water and ethanol and left to dry at room temperature. Figure 1 represents the schematic of the composite nanofiber membrane preparation.

Photodegradation experiments

The experiments were carried out by placing the NB crosslinked 3× 3 cm^2 nanofiber into a 9-cm diameter petri dish containing dye solution (50 mL) and continue shaking at 100 rpm on the orbital shaker. We started collecting the data, 30 min in the dark before switching the lamp on; afterwards, the solution was illuminated by a 500-W Halogen lamp which is located 50 cm away from the sample. A total of 2 mL of the dye solution was withdrawn from the dish after 30 min of dark shaking and then at a fixed interval of time and transferred to a glass tube and tested by using a UV-vis/NIR spectrophotometer to calculate the visible light photocatalytic degradation of the dye. All experiments were duplicated to assure the consistency and reproducibility of the results. The degradation efficiency of dyes was calculated by the following equation:

$$\text{Degradation efficiency } (\eta) = \left(\frac{C_0 - C}{C_0} \right) \times 100\%$$

where C_0 and C represent the dye concentration before and after irradiation and are measured in milligrams/l. To study the effect of pH, the degradation efficiency was investigated for different pH values of 4, 6, 8, and 10. The solution pH value is controlled by the addition of NaOH (0.1 M) and HCl (0.1 M) solution.

Characterization

Particle morphologies were measured by high-resolution transmission electron microscopy, HRTEM, JEM-2100, jeol. Scanning electron microscopy was carried out using FE SEM-Quanta FEG-250, Thermo Fisher Scientific, whereas the X-ray powder diffraction calculations were performed on D8 Discover, Bruker, where Cu-Kα radiation was used with wavelength of 1.540 Å. Fourier-transformed infrared spectroscopy spectra were recorded on Nicolet 6700 FTIR with smart ITR, Thermo Scientific. The contact angle of nanocomposite was measured by using One Attention Ver. 2.7 (r5433), Biolin Scientific. The UV-visible/NIR spectrophotometers for diffusion reflectance spectroscopy are obtained through the application of Jasco V570, JASCO. The dye's absorbance for MG ($\lambda_{max} = 617$ nm) and MB ($\lambda_{max} = 668$ nm) samples were recorded by using a single-beam visible spectrophotometer, Jenway 6300, Cole-Parmer, where deionized water has been used as a reference sample.

Results and discussion

Material characterization

We applied Bragg's law of diffraction at a specific group of planes with a known inter-planar distance to find the samples

Fig. 1. A schematic of the preparation techniques and the experimental procedure followed in this study
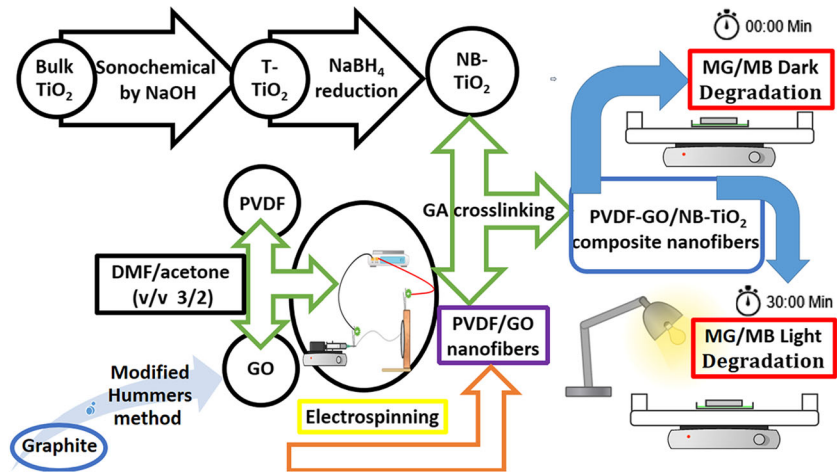
lattice constants (a, b, and c) from the XRD scans. Then, the unit cell volume (V) and the theoretical density D as given by $D = \frac{ZM}{N_A V}$, where Z is the number of molecules per unit cell, M is the molecular weight, and N_A is Avogadro's number, are directly calculated. Moreover, the average crystallite size (D_x) of the investigated samples was calculated by applying the Debye–Scherrer equation (Phokha et al. 2014): $D_x = \frac{k\lambda}{\beta \cos\Theta}$ where λ is the Cu-k_α wavelength, k is the shape factor, whose usual value is 0.89, β is the full width at half maximum (FWHM) in radians, and Θ is the diffraction angle. Table 1 shows that the structural parameters, specifically, the average crystallite size, the lattice constants, and the unit cell volume of the treated (T) sample, are slightly larger than those of the as-purchased anatase sample, while the nano-black TiO$_2$ (NB) displays the least average crystallite size; its lattice constants and unit cell volume relatively expand. Therefore, the NB density shows the minimum value of all samples.

Figure 2a shows the X-ray diffraction of the as-purchased, treated (T), and nano-black (NB) TiO$_2$. The scans demonstrate the crystallinity and the single-phase formation of the three oxides. XRD patterns show relatively strong diffraction peaks at around 25° and 48° which are indications of the anatase phase (Thamaphat and Limsuwan 2008; Ahmed et al. 2015). The NB-pattern shows relatively tiny peaks at diffraction angles of about 42.5°, and 46.0° and the shoulder at 31.0°, which correspond to the brookite phase. This is in agreement with

previous studies which confirmed that anatase may transform directly to brookite if the sample is heated in between 300 and 450 °C. Moreover, because of the surface distortion of the black-TiO$_2$, as will be demonstrated later, oxygen vacancies and/or Ti-interstitials are generated in the lattice. Eventually, these imperfections will promote microstrains in the crystal and subsequently produce changes in the lattice constants of the anatase (Hu et al. 2003). Figure 2b shows the deviation of the peak position around 25.6°. The peak shift of the T and NB samples is toward smaller angles. This is consistent with the variations of the lattice parameters in Table 1.

Figure 3 displays the X-ray diffraction of GO, PVDF nanofiber, PVDF-GO nanofiber (0.3% GO), and PVDF-GO/NB-TiO$_2$ (0.3% GO with 20 mg NB-TiO$_2$). For GO, a sharp peak at 10° was correlated to the (001) inter-layer structure of GO sheets (Xu et al. 2016). The PVDF nanofiber has strong two peaks at 20.3° and 18.5° which correspond to (110/101) and (020) of monoclinic crystal, respectively (Cai et al. 2017). For the composite nanofiber membrane, the diffraction peaks at 25.3°, 31.0°, 37.8°, 42.5°, 46.0°, 47.9°, 53.8°, 55.0°, and 62.9° can be indexed to the NB-TiO$_2$ (Mohamed et al. 2017a).

For the AP and T samples, Fig. 4a unveils that the transmittance is relatively low up to a wavenumber of about 730 cm^{-1}. In the range 800 to 4000 cm^{-1}, the transmittance is rather high for the as-purchased sample and even higher for the treated TiO$_2$, whereas the NB sample shows a peak of the

Table 1 Average crystal size (D_x), lattice constants, unit cell volume, and theoretical density for as purchased anatase, treated, and nano black TiO$_2$ samples.

TiO$_2$ sample.	Average grain size from (SEM) (nm)	Average crystallite size (D_X) (nm)	Lattice constants			Unit cell volume (v) (nm^3)	Theoretical density (D) (g/cm^3)
			a (nm)	b (nm)	c (nm)		
As purchased anatase (AP)		32.3	0.37607	0.37607	0.94378	0.13348	3.97427
Treated (T)	110±32	32.4	0.37689	0.37689	0.94572	0.13434	3.94887
Nano black (NB)	124±33	25.3	0.37772	0.37772	0.94809	0.13527	3.92173
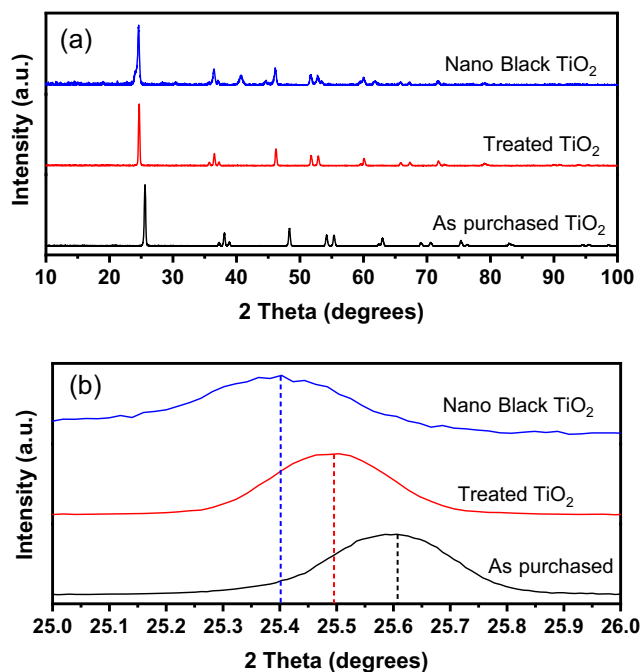
Fig. 2 a X ray diffraction of as purchased, treated (T), and nano black (NB) TiO$_2$. **b** Deviation of the peak position around 25.6°

transmittance at about 900 cm^{-1} and much lower values for higher wavenumbers. This means that the absorbance of NB-TiO$_2$ over the designated wavelength range is substantially higher than that of the other two samples. These observations may be explained by the dependence of the band intensity on the change of the dipole moment as a result of atoms displacement and on its degree of anharmonicity (Pasquini 2003; Mohamed et al. 2017a).

The functional groups of the investigated samples are inspected by FTIR. The fingerprint region of any FTIR spectrum lies in the range 400 to 1500 cm^{-1} since it is the usual range used to identify the dissimilar compounds. In this study,
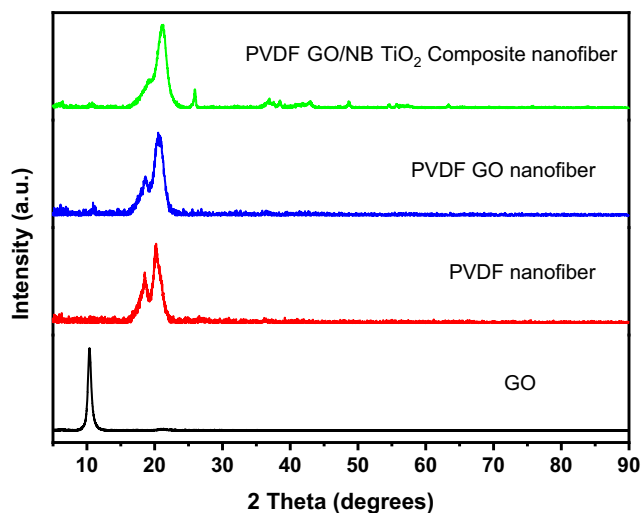
Fig. 3 XRD of GO, PVDF nanofiber, PVDF GO nanofiber, and PVDF GO/NB TiO$_2$

the first fingerprint band, around 725 cm^{-1}, is associated with the bond Ti-O-Ti in the anatase phase (Ullattil et al. 2018). Additionally, the other characteristic band at 915 cm^{-1} is ascribed to the Ti-O vibrations (Lohrasbi 2014). Knowing that, even at normal conditions, the TiO$_2$ surface interacts promptly with water, which in turn has a substantial influence on surface processes, such as photo-catalysis (Trimboli et al. 2006). Specifically, the band in the range 3800–3600 cm^{-1} is attributed to stretching vibrations of OH groups, besides various OH groups on TiO$_2$ are marked by the bands 3720 to 3620 cm^{-1} (Mohamed et al. 2017b). The band around 3600 cm^{-1} is indicative of a "free" OH group, and it may be residing on the surface, or encapsulated within the crystal lattice (Mantsch 2006). The spectra also display two prominent bands around 3400 (O-H stretching) and 1645 cm^{-1} (H-O-H) bending (Kong and Yu 2007). Moreover, the existence of moderate to intense bands in the ranges 1600–1300, 1200–1000, and 800–600 cm^{-1} is an indication of a simple hydroxyl compound. The nano-black sample displays in addition to the bands that correspond to Ti-O-Ti bond and Ti-O vibrations, an extra band, rather small, at around 3670 cm^{-1} due to hydrogenation (Mohamed et al. 2016b). Figure 4b shows the FTIR spectrum of GO bands at 1050, 1250, and 1403 cm^{-1} that correspond to C–O, C–O–C, and C–OH bonds, respectively. The resonance peak of the C–C stretching and the absorbed OH groups in the GO occurs at 1620 cm^{-1} (Krishnamoorthy et al. 2013). Generally, the band 1700–1600 cm^{-1} is due primarily to the C=O stretching vibration. And the two bands 3000 to 2800 cm^{-1} and 1500 to 1300 cm^{-1} correspond to C–H simple stretching and bending vibrations, respectively (Mantsch 2006). Moreover, the band around 2350 cm^{-1} designates chemisorbed CO$_2$ (Drouet et al. 2001). Generally, since the measurements are done in-air, the spectrum shows OH and CO functional groups as predicted (Xu et al. 2015). Fig. 4c displays the FTIR spectra of the GO, PVDF nanofiber, and PVDF nanofiber with 0.3 wt.% GO. The absorption bands of the α-phase appear at 764, 976, and 978 cm^{-1}, and the absorption bands for the β-phase exist at 842 and 1272 cm^{-1} (Abbasipour et al. 2017). The bending and wagging vibration of the CF$_2$ group and the rocking of the main PVDF chain are the most dominating peaks for the α-phase at 614 and 762 cm^{-1}, respectively (Issa et al. 2016). Doping with GO makes the peaks that correspond to the β-phase significantly stronger and sharper, while the peaks corresponding to the α-phase became fainter (Abbasipour et al. 2017). Therefore, GO causes the transformation from α- to β-crystalline phase (Issa et al. 2016). The utilization of GO as a nanofiller produced effective dipole polarization in the PVDF and eased the nucleation of β-phase crystals. Besides, both graphene and PVDF β-phase possess a carbon zigzag structure, which match with each other. CF$_2$ in PVDF interacts with the C=O and COOH groups of the GO (hydrophilic interaction). Moreover, the GO layers act as an obstructing agent for the
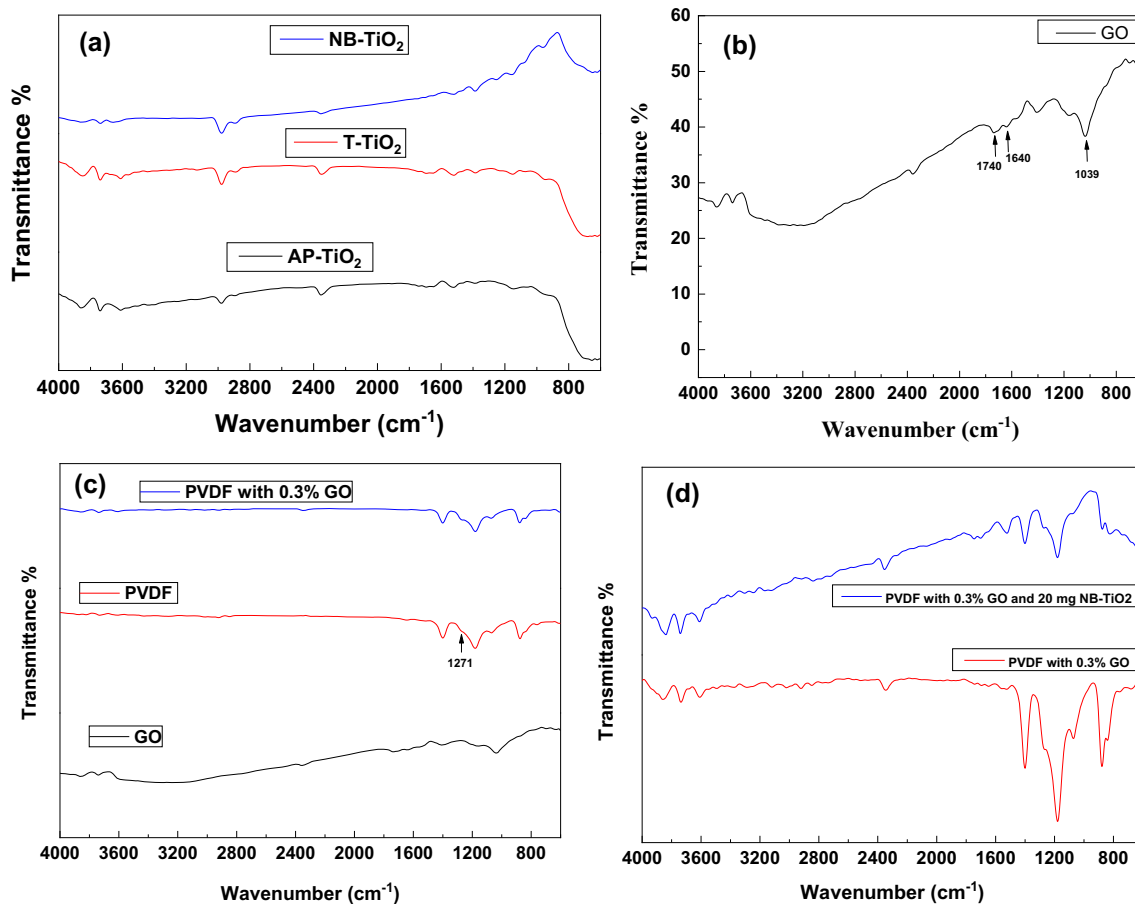
Fig. 4 FTIR of (**a**) AP, T, and NB TiO$_2$; (**b**) prepared GO; (**c**) GO, PVDF nanofiber, and PVDF nanofiber with 0 3% GO; and (**d**) PVDF nanofiber with 0.3% GO and PVDF nanofiber with 0.3% GO doped with 20 mg NB TiO$_2$

α-phase and as a nucleating agent for the β-phase (Abbasipour et al. 2017). The nanofibers with 0.3% of GO particles confirmed a β-phase because of the strong Van der Waals interactions between the highly electronegative fluorine on the PVDF chains and the free electron pairs on the GO oxygen atoms. This probably enforced the arrangement of the PVDF chains into a β-conformation when crystallizing on the GO surface (Issa et al. 2016). Figure 4d displays the FTIR of PVDF nanofiber with 0.3 wt.% GO with and without 20 mg of TiO$_2$.

Generally, HRTEM and FESEM are valuable at inspecting the morphology and the crystallinity of the sample, as well as the particle size. Depending on the synthesis procedure, dissimilar types of morphology were designated including nanotubes (Chen et al. 2014), wires (Wang and Chou 2016), spheres (Panomsuwan et al. 2015), and spikes (Sanz et al. 2015). A defective surface layer of hydrogenated TiO$_2$, as well as a crystalline core and amorphous shell structure, has been confirmed by many researchers. The common observed defects on the black-TiO$_2$ surface are Ti^{3+} ions and oxygen vacancies (Mohamed et al. 2016a). For HRTEM imaging, the specimens were prepared by ultra-sonicating the powder samples in ethanol for 15 min prior to measurements to ensure

uniform distribution. HRTEM micrographs, Fig. 5a, b, and c, display the treated and NB samples as aggregates of irregular particles. The aggregation is denser for the treated sample, whereas the NB particles have a relatively larger size. Furthermore, Fig. 5d and e demonstrate the scanning electron microscope images of the two samples. Both samples show a porous brain-like morphology of accumulated non-uniform particles with different sizes, and the insets display the histograms of the samples. The average particle diameters are 110 ± 32 and 124 ± 33 nm for the treated and the NB samples, respectively. The difference between the XRD crystallite size and FESEM particle size may be explained as a result of small crystal accumulation to attain a lower free-energy state. Whenever the adjacent surfaces share the same crystallographic orientation, the adjacent interfaces are eliminated, and the nanoparticles are combined together into a larger particle (Kibasomba et al. 2018). Moreover, the inter-particle interaction has also its vital role in the abovementioned discrepancy.

The corresponding selected area electron diffraction (SAED) patterns of treated and NB-TiO$_2$ powders are shown in Fig. 6a and b, respectively. The SAED patterns of the NB sample show more diffraction spots and rings of second
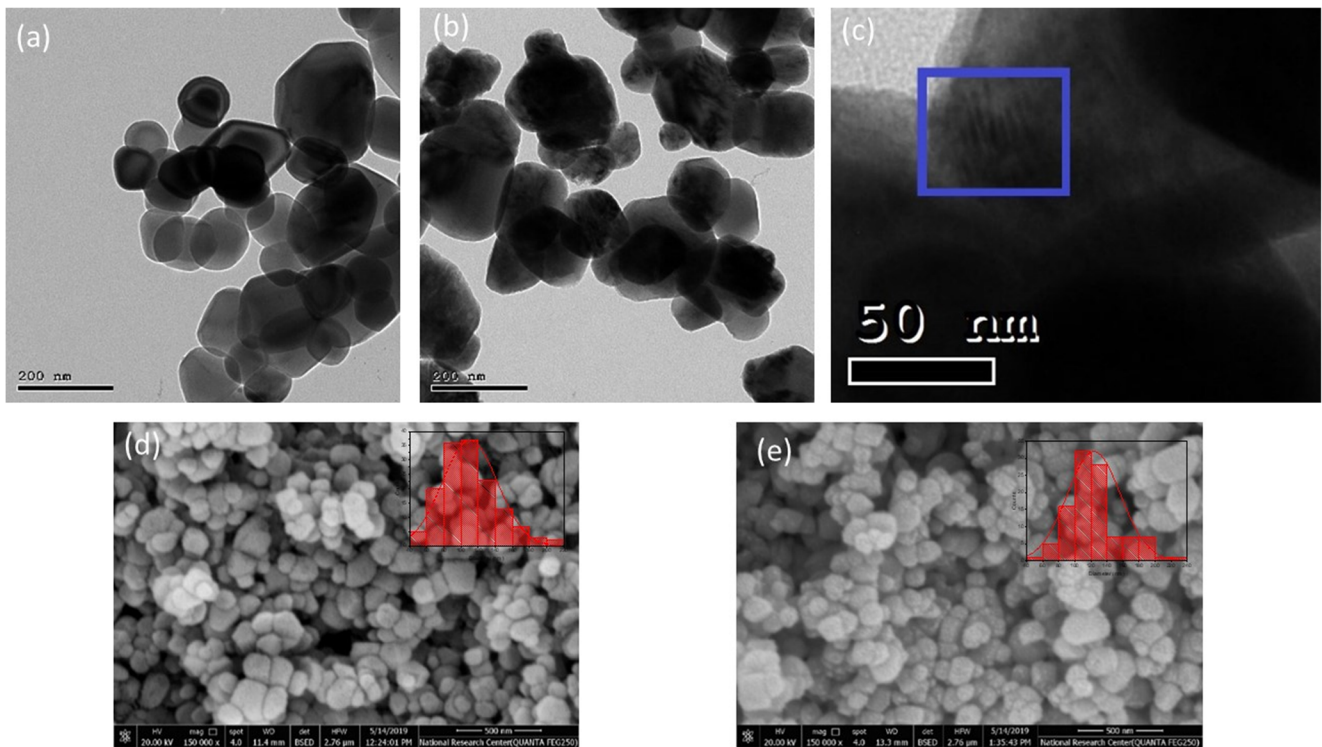
Fig. 5 HRTEM of (**a**) T TiO$_2$, (**b**) NB TiO$_2$, and (**c**) Moiré fringes in NB sample; FESEM of (**d**) treated and (**e**) NB TiO$_2$ nanoparticles, with the corresponding particles distribution as insets

phases whose brightness is much fainter, so they are badly crystallized and/or partly amorphous (Cheng et al. 2015). The crystallinity may also be checked by Moiré patterns and their corresponding line analysis. Figure 5c illustrates the Moiré patterns for the NB-TiO$_2$ sample. Figure 7a and c demonstrate the corresponding HRTEM micrograph and line analysis for the treated sample. In contrast to the black sample, the treated sample shows a regular line analysis which indicates no surface distortion, whereas Fig. 7b indicates surface distortion for the NB sample. This is even emphasized by its irregular line analysis, Fig. 7d.

The SEM micrographs in Fig. 8a and b illustrate the adhesion of GO flakes on the PVDF nanofibers' surface. Clearly, the micrographs display that GO flakes are intermingled with the nanofibers. The nanofibers seem denser for the pure PVDF polymer. The two micrographs consist of non-uniform fibers, but the degree of non-uniformity is greater for the PVDF-GO hybrid. The average diameters are calculated from the fiber histograms in Fig. 8a and b as 480 and 358 nm for the pure polymeric and hybrid nanofibers, respectively. Generally, the nanofiber diameter and morphology depend on many polymeric solution parameters like viscosity, surface tension,

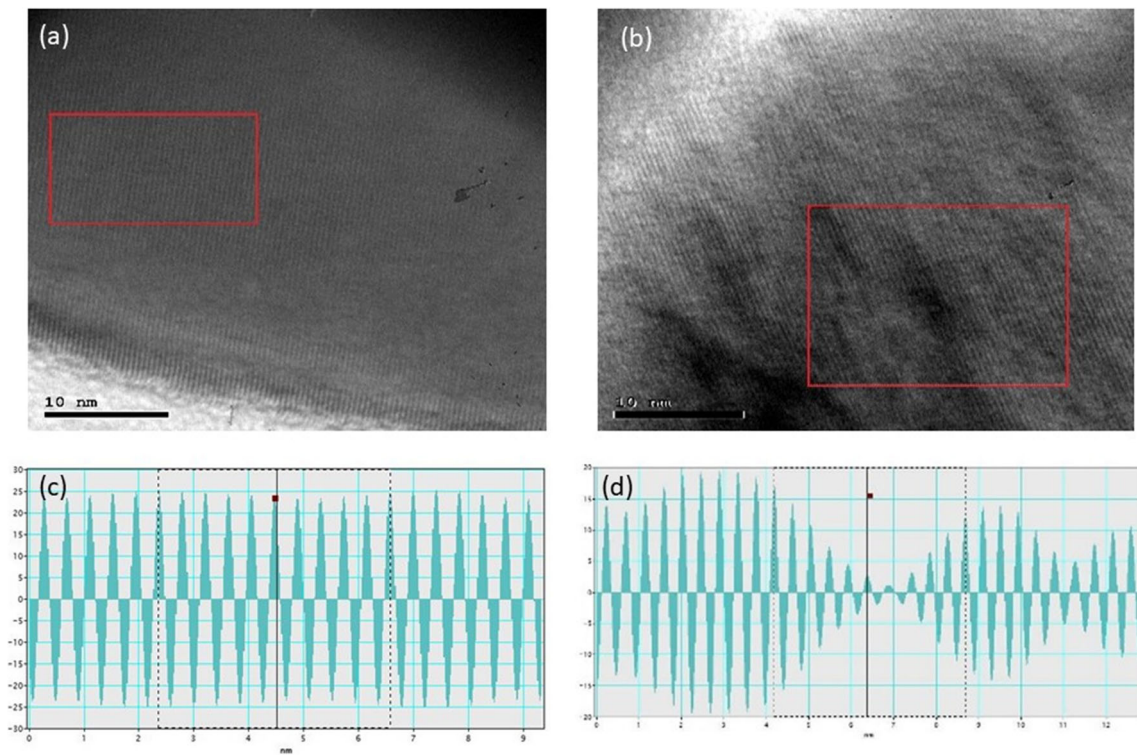**Fig. 6** SAED patterns of (**a**) treated and (**b**) NB TiO$_2$ samples
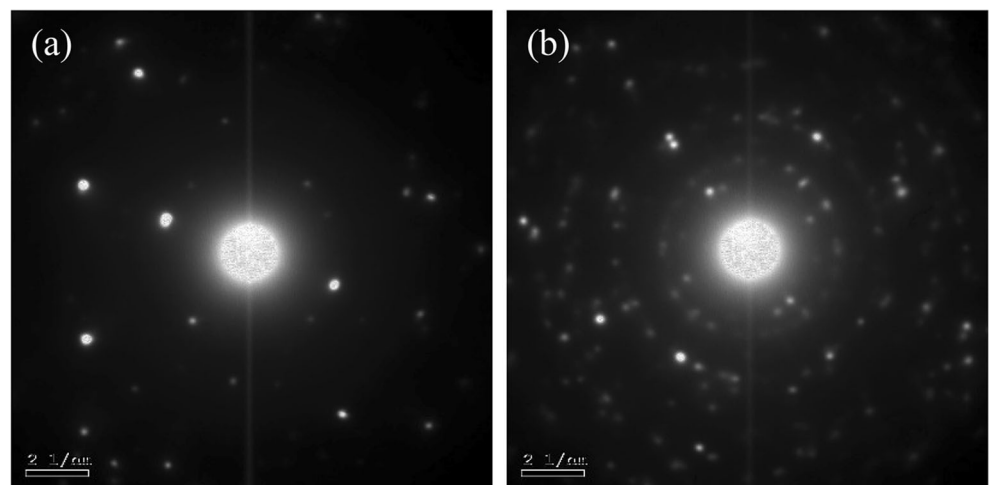
Fig. 7 HRTEM micrographs and line analysis of (**a** and **c**) treated and (**b**, **d**) NB TiO$_2$
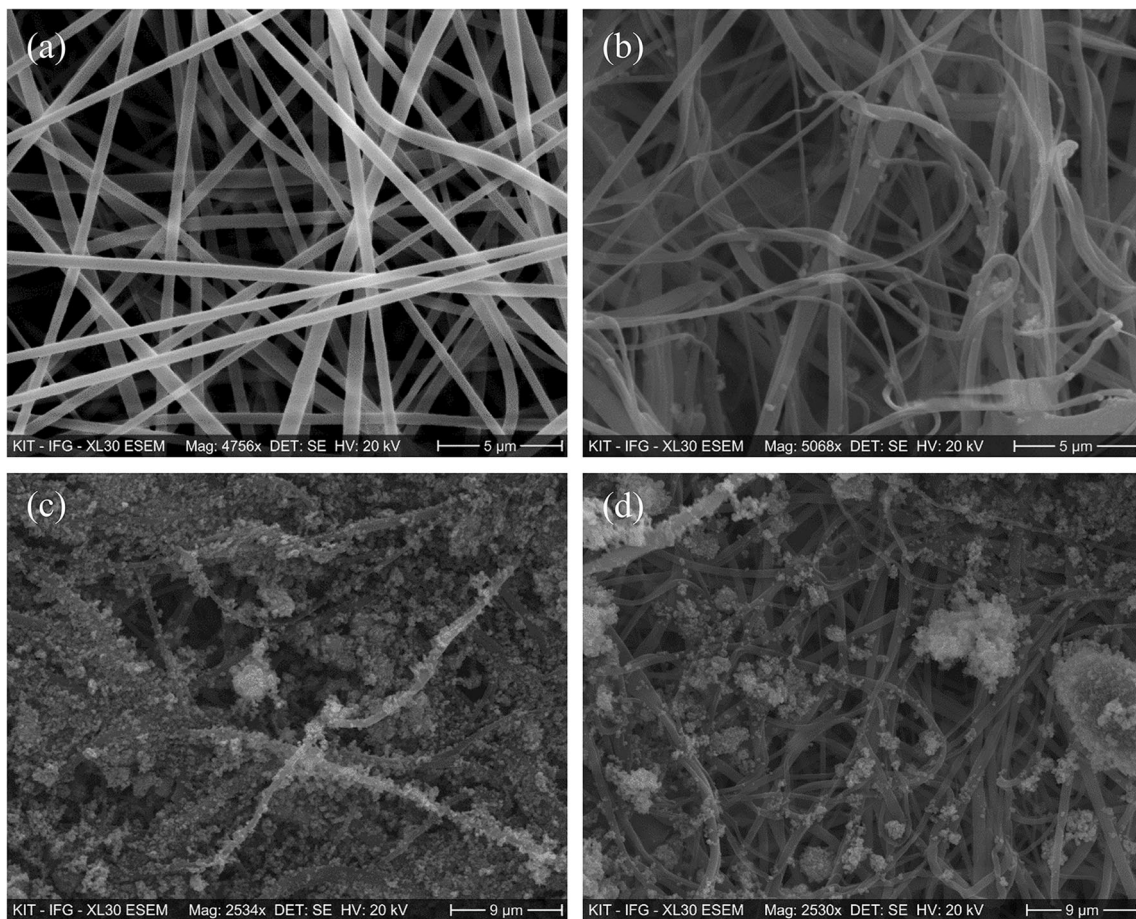

Fig. 8 FESEM of (**a**) PVDF nanofiber, (**b**) PVDF nanofiber with 0.3% GO, (**c**) and (**d**) PVDF GO/NB TiO$_2$ composite nanofibers

temperature, electrical conductivity, and concentration. Moreover, they are also influenced by device parameters like high voltage value, tip-collector distance, and the collector rotational speed. Specifically, increasing the net charge density and the surface tension coefficient favors the formation of smaller diameter fibers (H. Fong 1999), where the net charge density = jet current × collecting time × concentration × solution density/mass of dry polymer. On the other hand, the polymer jet becomes highly unstable at higher voltage, and thicker fibers are formed but with a high standard deviation of the fiber diameter, which is a consistent description of our data (Motamedi et al. 2017). Moreover, the hybrid fibers show several scattered beads. Typically, the solution viscosity, surface tension, and the net charge density of the electrospinning jet are the main factors of electrospun bead formation (Fong et al. 1999). Figure 8c and d show the FESEM of PVDF-GO/NB-TiO$_2$ composite nanofibers after crosslinking PVDF-GO composite nanofiber with NB-TiO$_2$. The morphology of the surface shows that NB-TiO$_2$ stacks on the surface of PVDF-GO composite nanofiber.

The contact angle is designated as the interface angle between the liquid and contact surfaces. Generally, the degree of wettability of a solid by a liquid is directly measured by the average contact angle. Whenever the contact angle tends to zero, this is referred to as complete wetting, whereas it is either wettable (hydrophilic) or non-wettable (hydrophobic) depending on whether the angle is smaller or greater than 90°, respectively (Ray et al. 2018). Figure 9 demonstrates water droplets on top of nanofibers for the pure PVDF, PVDF-GO, and PVDF-GO/NB-TiO$_2$ composite nanofibers. The average contact angle measurements indicate that the hybrid PVDF nanofiber with 0.3% GO and 20 mg NB-TiO$_2$ displays the highest contact angle (138.6°), whereas the lowest contact angle (129.2°) occurs for PVDF nanofiber with 0.3 wt.% GO. The pure PVDF nanofiber shows a contact angle of 131.7°. It is well-known that TiO$_2$ is itself a hydrophobic material; therefore, its loading to the membrane will increase the contact angle, as expected. However, the effect of adding such a tiny amount of titania is causing merely 7.3% increase of the contact angle.

Davis and Mott (Davis 2012) extended Tauc et al.'s (Tauc 1969) proposition of applying the optical absorbance data to find the band gap energy. They argued that the absorption coefficient α is related to the band gap energy E_g as $(\alpha h \nu)^{\frac{1}{n}} = A \left(h\nu - E_g \right)$ where h is Planck's constant, υ is the photon frequency, A is a constant, and n refers to the nature of the electronic transition. Where the allowed direct, indirect transitions are denoted by $n = 1/2, 2$; and $n = 3/2, 3$ for the forbidden direct, indirect transitions, respectively. The absorption processes are normally dominated by the allowed transitions (Viezbicke et al. 2015). The absorption coefficient, α, is calculated from the absorbance, Abs, using the relation, $\alpha = \ln 10^{Abs}$ per unit length of the absorbing material (Tański et al. 2016). The absorbance measurements of treated and black TiO$_2$ are shown in Fig. 10a. The absorbance of the NB sample is greatly enhanced relative to that of the treated sample in the UV and visible regions. The spectra of the NB- and T samples display two main UV peaks at 195 and 275 nm. There is no noticeable relative shift in the two peaks for the two samples. Kubelka-Munk theory was applied to calculate the energy gap from UV-vis diffuse reflectance spectra. A uniform diffuse irradiation is assumed to propagate through a one-dimensional isotropic slab, assuming no reflection at the boundaries [44, 45]. The Kubelka-Munk function (KMF), $F(R_\infty)$, may be written as (Motamedi et al. 2017): $F(R_\infty) \equiv \frac{(1-R_\infty)^2}{2R_\infty}$, where R_∞ is the reflectance of an infinitely thick layer for which an additional increase in thickness does not alter its reflectance. This is attained for fine powders at only a few millimeters depth. The KMF is easily formulated as $F(R_\infty) = \frac{K}{S}$, where K and S are the absorption and scattering coefficients, respectively. Moreover, the KMF and the energy band are correlated as $h F(R_\infty) \alpha (h - E_g)^n$. The four values of n coincide with the allowed and forbidden transitions mentioned above. Finally, to find E_g, assuming allowed direct transition, a graph of $[\alpha h\nu]^2$ or $[h\nu F(R_\infty)]^2$ is plotted versus $h\nu$, following Tauc's method or Kebulka-Munk theory, respectively. These two graphs are represented in Fig. 10b and c. The intersection of the extrapolated linear portion of the graph with $h\nu$ axis gives the optical energy band. Figure 10d shows a summary of the attained optical energy gap values.
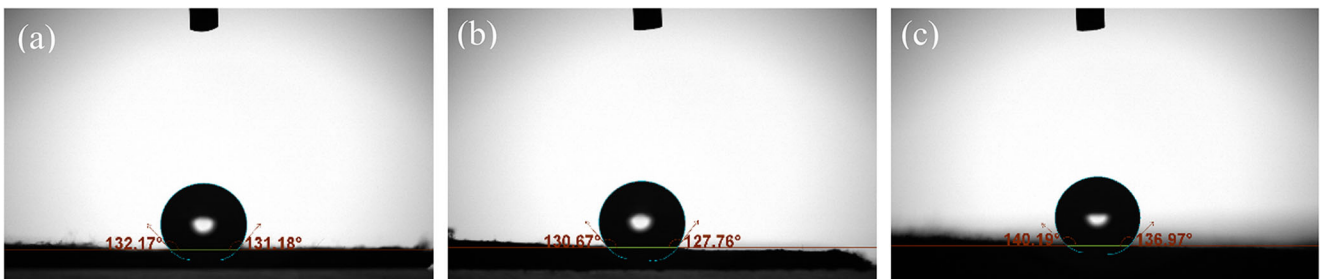

Fig. 9 Contact angle measurements for (**a**) pure PVDF nanofiber, (**b**) PVDF GO nanofiber, and (**c**) PVDF GO/NB TiO$_2$ composite nanofiber
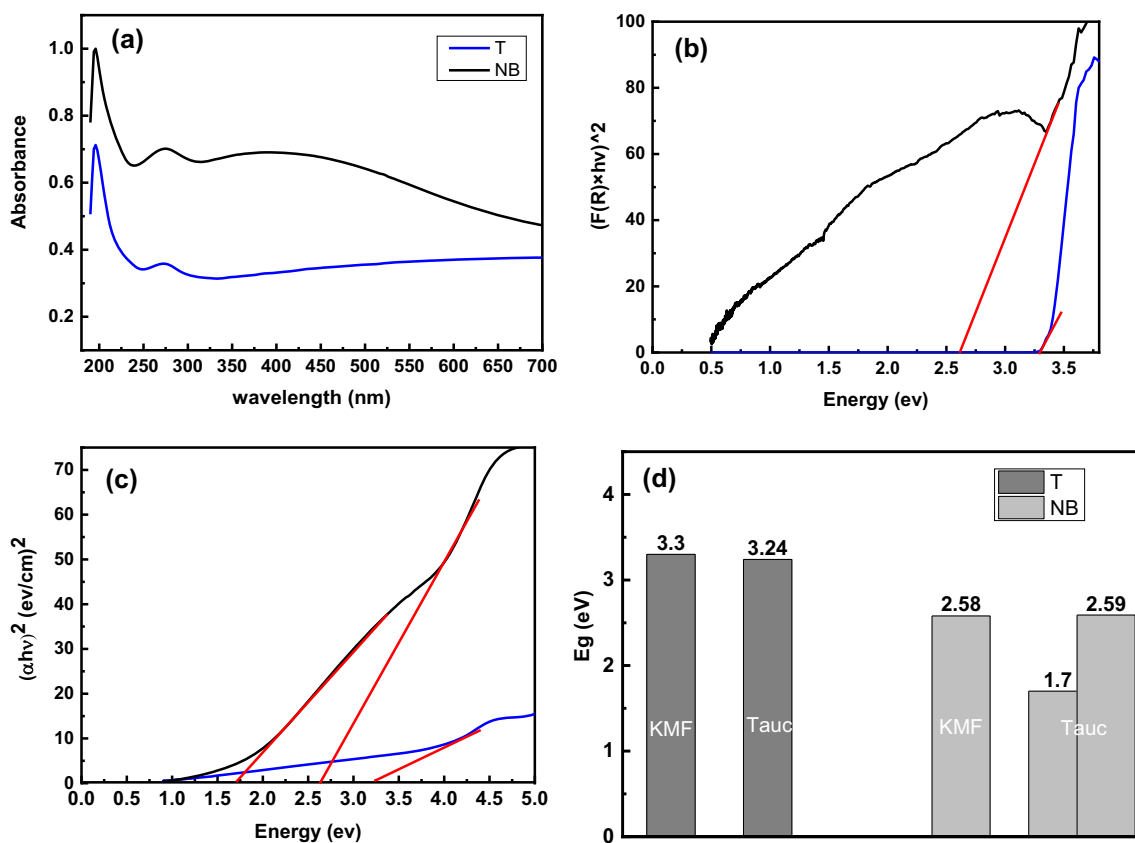
Fig. 10 Optical investigation of T and NB TiO$_2$ (**a**) absorbance variation with wavelength; energy gap, assuming allowed direct transition, from (**b**) KMF and (**c**) Tauc plots; (**d**) summary of acquired energy gap values

Photocatalytic degradation of MG and MB over NB-TiO$_2$ composite nanofibers

In order to explore the effective photodegradation under visible light irradiation, different catalyst quantities range from 5 to 20 mg were carried out (Fig. 11a). The maximum degradation of 74 and 39% was obtained at 20 mg of the catalyst and 30 min contact time for MG and MB, respectively. The result shows that the higher amount of catalyst provides higher photodegradation efficiency due to the increase of the surface area and the number of active sites available (Mohamed et al. 2019a). Different dye pH values of 4, 6, 8, and 10 for 30 min, 5 mg/L of MB and MG and 20 mg NB-TiO$_2$ were investigated to reveal the optimum degradation efficiency as shown in Fig. 10b. The result shows that pH 8 is the maximum for MG, and pH 10 is the maximum for MB. Furthermore, the effect of dye concentration on degradation efficiency was performed by increasing the concentration to 10 mg/L (Fig. 11d and e). The results reveal that no significant change in degradation efficiency namely decreasing 10%. MB shows a better dark degradation; however, the photocatalytic degradation is much better for MG. The dye concentration decays monotonically and almost vanished in 120 min. These results are attributed to the limitation of hydroxyl radicals and the

occupation of the active sites (Mohamed et al. 2017c; Khalil and Schäfer 2021).

Incident photons on NB-TiO$_2$ with quantized energy ($h\nu$) equals to or exceeds the excitation energy (E_g) will produce electron-hole pairs. As a result of this photo-induced process, (e$^-$/h$^+$) pairs may be transferred to the NB-TiO$_2$ surface and become involved in two pathways. These redox reactions could be summarized as shown in Fig. 12b. The main outcome of the two paths is the powerful oxidizing agent, $OH^\bullet$, as presented in Fig. 12a, which will subsequently interact chemically with the pollutants and transform them into harmless compounds. Hydroxyl groups on NB-TiO$_2$ profoundly affect its electronic properties and surface chemistry. These surface groups exceptionally affect the charge separation and diffusion of photogenerated electrons and holes which remarkably enhances the photodegradation process. Hydroxyl radicals are produced in the first path as the hole reacts with water and hydroxide ions and in the second path as the electron reacts with oxygen to produce intervening superoxide radical anions and hydrogen peroxide which ultimately produce hydroxyl radicals as well. Finally, the pollutants adsorbed on the surface of NB-TiO$_2$ will be dissolved rapidly by the hydroxyl radicals into intermediates which in turn decompose to safe byproducts like CO$_2$ and H$_2$O.
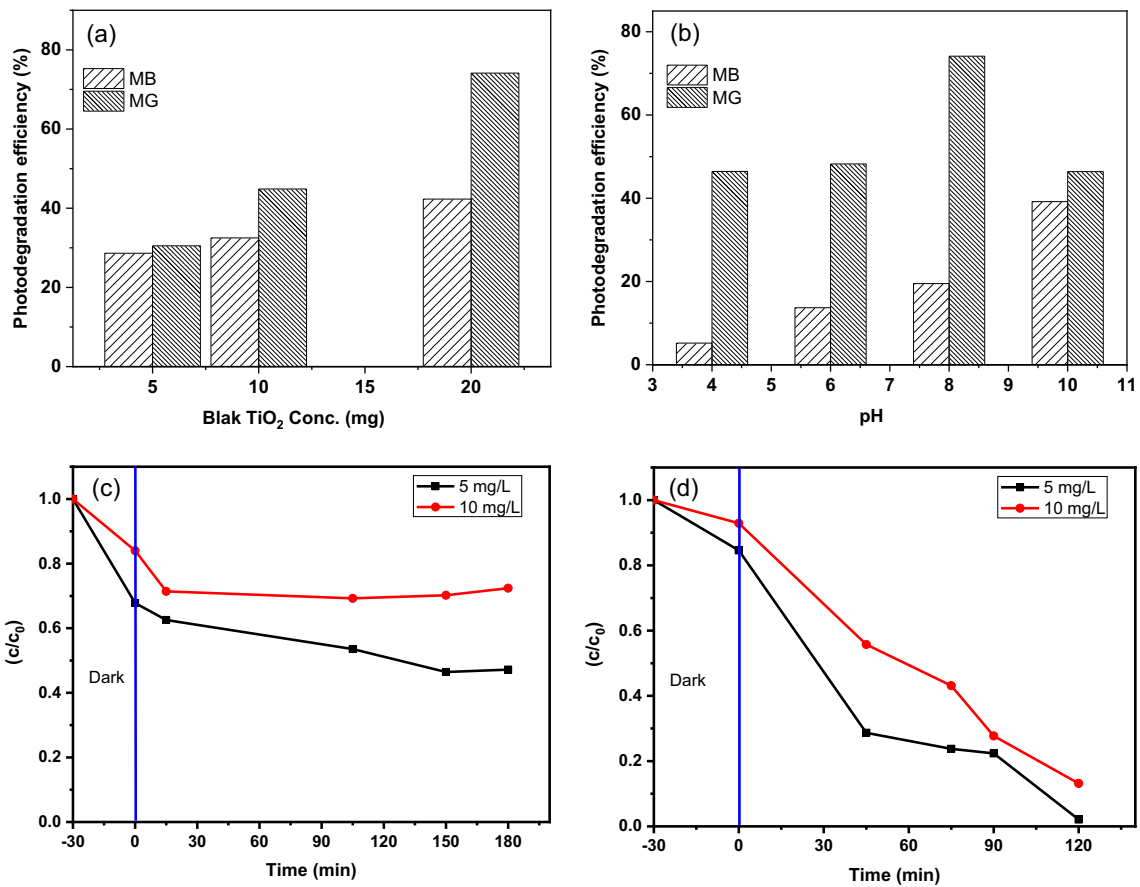
Fig. 11 (**a**) Effect of catalyst amount (5 mg/L, 30 min, and pH 7), (**b**) effect of pH (5 mg/L, 30 min, and 20 mg), photodegradation of (**c**) MB (pH 10), and (**d**) MG (pH 8)

Conclusions

The nano-black TiO$_2$, GO, and the prescribed membranes were successfully synthesized with no secondary phases recorded. Meanwhile, the HRTEM micrographs and corresponding line analysis clearly displays the black titania surface distortion, repeatedly indicated in the literature. Likewise, the SAED patterns of NB sample reflect its bad crystallinity and even being partly amorphous as may be anticipated from

the relatively more diffraction spots and rings of second phases whose brightness is much fainter. Moreover, a percentage drop of at least 20% is reported for the optical energy gap as a result of transforming titanium dioxide into black TiO$_2$. The degradation of MG and MB depends upon all the reaction parameters such as catalyst amount, pH, and dye concentration. Furthermore, using the composite nanofiber membrane under visible light for 30 min, the photocatalytic degradation efficiencies of MG and MB were found to be 74 and 39%,
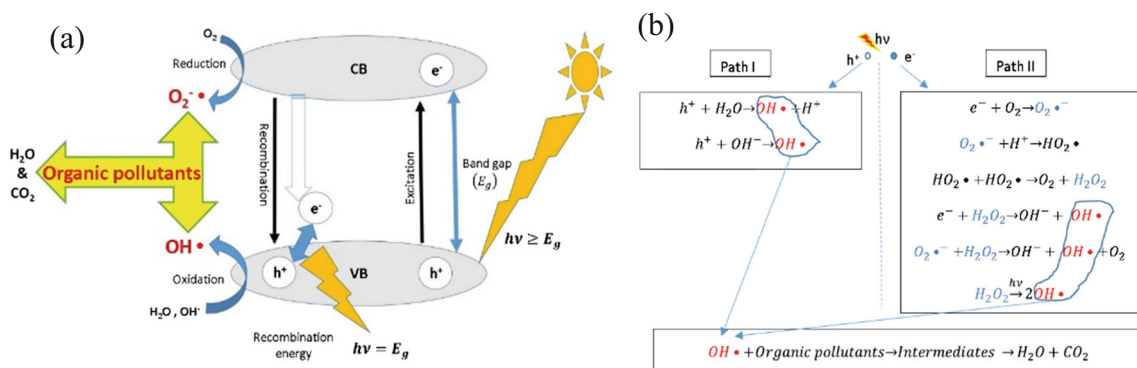

Fig. 12 (**a**) A schematic of photocatalytic degradation of organic pollutants on NB TiO$_2$ in the presence of solar light, and (**b**) a summary of the redox reactions at the surface of NB TiO$_2$

respectively. The excellent visible photocatalytic activity for MB and MG degradation has been due to its unique narrow energy gap between the oxygen vacancy state and the conduction band, ensuring its excellent visible light absorption to produce photoelectrons and holes in NB-TiO$_2$.

Declarations

References

Abbasipour M, Khajavi R, Yousefi AA, Yazdanshenas ME, Razaghian F (2017) The piezoelectric response of electrospun PVDF nanofibers with graphene oxide, graphene, and halloysite nanofillers: a comparative study. J Mater Sci Mater Electron 28(21):15942 15952

Abdel Mottaleb MM, Khalil A, Karim S, Osman TA, Khattab A (2019a) High performance of PAN/GO ZnO composite nanofibers for photocatalytic degradation under visible irradiation. J Mech Behav Biomed Mater 96:118 124

Abdel Mottaleb MM, Khalil A, Osman TA, Khattab A (2019b) Removal of hexavalent chromium by electrospun PAN/GO decorated ZnO. J Mech Behav Biomed Mater 98:205 212

Aboamera NM, Mohamed A, Salama A, Osman TA, Khattab A (2018) An effective removal of organic dyes using surface functionalized cellulose acetate/graphene oxide composite nanofibers. Cellulose 25(7):4155 4166

Aboamera NM, Mohamed A, Salama A, Osman TA, Khattab A (2019) Characterization and mechanical properties of electrospun cellulose acetate/graphene oxide composite nanofibers. Mech Adv Mater Struct 26(9):765 769

Ahmed MA, Imam NG, Abdelmaksoud MK, Saeid YA (2015) Magnetic transitions and butterfly shaped hysteresis of Sm Fe Al based perovskite type orthoferrite. J Rare Earths 33(9):965 971

Arami H, Mazloumi M, Khalifehzadeh R, Sadrnezhaad S (2007) Sonochemical preparation of TiO2 nanoparticles. Mater Lett 61(23 24):4559 4561

Bai J, Zhou B (2014) Titanium dioxide nanomaterials for sensor applications. Chem Rev 114(19):10131 10176

Batzill M, Morales EH, Diebold U (2006) Influence of nitrogen doping on the defect formation and surface properties of TiO$_2$ rutile and anatase. Phys Rev Lett 96(2):026103

Cai X, Lei T, Sun D, Lin L (2017) A critical analysis of the α, β and γ phases in poly(vinylidene fluoride) using FTIR. RSC Adv 7(25):15382 15389

Castkova K, Kastyl J, Sobola D, Petrus J, Stastna E, Riha D, Tofel P (2020) Structure properties relationship of electrospun PVDF fibers. Nanomaterials (Basel, Switzerland) 10(6):1221

Chalastara K, F G, Elouatik S, Demopoulos GP (2020) Tunable composition aqueous synthesized mixed phase TiO2 nanocrystals for photo assisted water decontamination: comparison of anatase, brookite and rutile photocatalysts. Catalysts 10(4):407

Chen X, Liu L, Yu PY, Mao SS (2011) Increasing solar absorption for photocatalysis with black hydrogenated titanium dioxide nanocrystals. Science 331(6018):746 750

Chen B, Beach JA, Maurya D, Moore RB, Priya S (2014) Fabrication of black hierarchical TiO2 nanostructures with enhanced photocatalytic activity. RSC Adv 4(56):29443 29449

Cheng G, Xu F, Stadler FJ, Chen R (2015) A facile and general synthesis strategy to doped TiO2 nanoaggregates with a mesoporous structure and comparable property. RSC Adv 5(79):64293 64298

Davis, N. F. M. a. E. A. (2012). Electronic processes in non crystalline materials, Oxford Classic Texts in the Physical Sciences

Drouet C, Alphonse P, Rousset A (2001) IR spectroscopic study of NO and CO adsorptions on nonstoichiometric nickel copper manganites. Phys Chem Chem Phys 3(17):3826 3830

El Sherbiny S, Morsy F, Samir M, Fouad OA (2014) Synthesis, characterization and application of TiO2 nanopowders as special paper coating pigment. Appl Nanosci 4(3):305 313

Fong H, C I, Reneker DH (1999) Beaded nanofibers formed during electrospinning. Polymer 40:4585 4592

Hu Y, Tsai H L, Huang C L (2003) Effect of brookite phase on the anatase rutile transition in titania nanoparticles. J Eur Ceram Soc 23(5):691 696

Issa AA, Al Maadeed MAAS, Mrlík M, Luyt AS (2016) Electrospun PVDF graphene oxide composite fibre mats with tunable physical properties. J Polym Res 23(11)

Karim SA, Mohamed A, Abdel Mottaleb MM, Osman TA, Khattab A (2018) Mechanical properties and the characterization of polyacrylonitrile/carbon nanotube composite nanofiber. Arab J Sci Eng 43(9):4697 4702

Karim SA, Mohamed A, Abdel Mottaleb MM, Osman TA, Khattab A (2019) Visible light photocatalytic activity of PAN CNTs/ZnO NH2 electrospun nanofibers. J Alloys Compd 772:650 655

Khalil AM, Schäfer AI (2021) Cross linked β cyclodextrin nanofiber composite membrane for steroid hormone micropollutant removal from water. J Membr Sci 618:118228

Khalil A, Aboamera NM, Nasser WS, Mahmoud WH, Mohamed GG (2019a) Photodegradation of organic dyes by PAN/SiO2 TiO2 NH2 nanofiber membrane under visible light. Sep Purif Technol 224:509 514

Khalil A, Nasser WS, Osman TA, Toprak MS, Muhammed M, Uheida A (2019b) Surface modified of polyacrylonitrile nanofibers by TiO2/MWCNT for photodegradation of organic dyes and pharmaceutical drugs under visible light irradiation. Environ Res 179:108788

Kibasomba PM, Dhlamini S, Maaza M, Liu C P, Rashad MM, Rayan DA, Mwakikunga BW (2018) Strain and grain size of TiO2 nano particles from TEM, Raman spectroscopy and XRD: the revisiting of the Williamson hall plot method. Results in Physics 9:628 635

Kong J, Yu S (2007) Fourier transform infrared spectroscopic analysis of protein secondary structures. Acta Biochim Biophys Sin 39(8):549 559

Krishnamoorthy K, Veerapandian M, Yun K, Kim SJ (2013) The chemical and structural analysis of graphene oxide with different degrees of oxidation. Carbon 53:38 49

Lohrasbi, M. (2014). In situ FTIR study of the photocatalytic properties of TiO2 and conductivity of polyaniline, University of Akron

Mantsch, R. A. S. H. H. (2006). Infrared spectroscopy in clinical and diagnostic analysis. Encyclopedia of Analytical Chemistry

Mapukata S, Hainer AS, Lanterna AE, Scaiano JC, Nyokong T (2020) Decorated titania fibers as photocatalysts for hydrogen generation

and organic matter degradation. J Photochem Photobiol A Chem 388:112185

Mendonça CD, Rahemi V, Hereijgers J, Breugelmans T, Machado SAS, De Wael K (2020) Integration of a photoelectrochemical cell in a flow system for quantification of 4 aminophenol with titanium di oxide. Electrochem Commun 117:106767

Mohamed, A. (2019). Chapter eight synthesis, characterization, and applications carbon nanofibers. Carbon based nanofillers and their rubber nanocomposites. S. Yaragalla, R. Mishra, S. Thomas, N. Kalarikkal and H. J. Maria, Elsevier: 243 257

Mohamed A, El Sayed R, Osman TA, Toprak MS, Muhammed M, Uheida A (2016a) Composite nanofibers for highly efficient photo catalytic degradation of organic dyes from contaminated water. Environ Res 145:18 25

Mohamed A, Osman TA, Toprak MS, Muhammed M, Yilmaz E, Uheida A (2016b) Visible light photocatalytic reduction of Cr(VI) by sur face modified CNT/titanium dioxide composites nanofibers. J Mol Catal A Chem 424:45 53

Mohamed A, Nasser WS, Osman TA, Toprak MS, Muhammed M, Uheida A (2017a) Removal of chromium (VI) from aqueous solu tions using surface modified composite nanofibers. J Colloid Interface Sci 505:682 691

Mohamed A, Osman TA, Toprak MS, Muhammed M, Uheida A (2017b) Surface functionalized composite nanofibers for efficient removal of arsenic from aqueous solutions. Chemosphere 180:108 116

Mohamed A, Yousef S, Ali Abdelnaby M, Osman TA, Hamawandi B, Toprak MS, Muhammed M, Uheida A (2017c) Photocatalytic deg radation of organic dyes and enhanced mechanical properties of PAN/CNTs composite nanofibers. Sep Purif Technol 182:219 223

Mohamed A, Ghobara MM, Abdelmaksoud MK, Mohamed GG (2019a) A novel and highly efficient photocatalytic degradation of malachite green dye via surface modified polyacrylonitrile nanofibers/ biogenic silica composite nanofibers. Sep Purif Technol 210:935 942

Mohamed A, Nasser WS, Kamel BM, Hashem T (2019b) Photodegradation of phenol using composite nanofibers under visi ble light irradiation. Eur Polym J 113:192 196

Motamedi AS, Mirzadeh H, Hajiesmaeilbaigi F, Bagheri Khoulenjani S, Shokrgozar M (2017) Effect of electrospinning parameters on mor phological properties of PVDF nanofibrous scaffolds. Progress in Biomaterials 6(3):113 123

Panomsuwan G, Watthanaphanit A, Ishizaki T, Saito N (2015) Water plasma assisted synthesis of black titania spheres with efficient visible light photocatalytic activity. Phys Chem Chem Phys 17(21):13794 13799

Park YR, Kim KJ (2005) Structural and optical properties of rutile and anatase TiO2 thin films: effects of co doping. Thin Solid Films 484(1):34 38

Pasquini C (2003) Near infrared spectroscopy: fundamentals, practical aspects and analytical applications. J Braz Chem Soc 14:198 219

Phokha S, Pinitsoontorn S, Maensiri S, Rujirawat S (2014) Structure, optical and magnetic properties of LaFeO3 nanoparticles prepared by polymerized complex method. J Sol Gel Sci Technol 71(2):333 341

Rajaraman TS, Parikh SP, Gandhi VG (2020) Black TiO2: a review of its properties and conflicting trends. Chem Eng J 389:123918

Ray, S. S., S. S. Chen, H. M. Chang, C. N. Dan Thanh, H. Quang Le and N. C. Nguyen (2018). "Enhanced desalination using a three layer OTMS based superhydrophobic membrane for a membrane distilla tion process." RSC Adv 8(18): 9640 9650

Ruan L, Y X, Chang Y, Zhou L, Qin G, Zhang X (2018) Properties and applications of the β phase poly(vinylidene fluoride). Polymers (Basel) 10(3):228

Salama A, Mohamed A, Aboamera NM, Osman T, Khattab A (2018) Characterization and mechanical properties of cellulose acetate/ carbon nanotube composite nanofibers. Adv Polym Technol 37(7): 2446 2451

Salimi A, Yousefi AA (2003) Analysis method: FTIR studies of β phase crystal formation in stretched PVDF films. Polym Test 22(6):699 704

Sanz R, Romano L, Zimbone M, Buccheri MA, Scuderi V, Impellizzeri G, Scuderi M, Nicotra G, Jensen J, Privitera V (2015) UV black rutile TiO2: an antireflective photocatalytic nanostructure. J Appl Phys 117(7):074903

Smijs TG, Pavel S (2011) Titanium dioxide and zinc oxide nanoparticles in sunscreens: focus on their safety and effectiveness. Nanotechnol Sci Appl 4:95 112

Sudova E, M J, Svobodova Z, Vesely T (2007) Negative effects of mal achite green and possibilities of its replacement in the treatment of fish eggs and fish: a review. Veterinarni Medicina 52(12):527 539

Tański T, Matysiak W, Hajduk B (2016) Manufacturing and investigation of physical properties of polyacrylonitrile nanofibre composites with SiO2, TiO2 and Bi2O3 nanoparticles. Beilstein Journal of Nanotechnology 7:1141 1155

Tauc, J. (1969). Optical properties and electronic structure of amorphous semiconductors. optical properties of solids: papers from the NATO Advanced Study Institute on Optical Properties of Solids Held August 7 20, 1966, at Freiburg, Germany. S. Nudelman and S. S. Mitra. Boston, MA, Springer US: 123 136

Thamaphat, K. and P. Limsuwan (2008). Phase characterization of TiO2 powder by XRD and TEM

Trimboli J, Mottern M, Verweij H, Dutta PK (2006) Interaction of water with titania: implications for high temperature gas sensing. J Phys Chem B 110(11):5647 5654

Ullattil SG, Narendranath SB, Pillai SC, Periyat P (2018) Black TiO2 nanomaterials: a review of recent advances. Chem Eng J 343:708 736

Viezbicke, B. D., S. Patel, B. E. Davis and D. P. Birnie III (2015). "Evaluation of the Tauc method for optical absorption edge deter mination: ZnO thin films as a model system." physica status solidi (b) 252(8): 1700 1710

Wang C C, Chou P H (2016) Effects of various hydrogenated treatments on formation and photocatalytic activity of black TiO2nanowire arrays. Nanotechnology 27(32):325401

Xu C, Shi X, Ji A, Shi L, Zhou C, Cui Y (2015) Fabrication and charac teristics of reduced graphene oxide produced with different green reductants. PLoS One 10(12):e0144842

Xu Z, Wu T, Shi J, Teng K, Wang W, Ma M, Li J, Qian X, Li C, Fan J (2016) Photocatalytic antifouling PVDF ultrafiltration membranes based on synergy of graphene oxide and TiO2 for water treatment. J Membr Sci 520:281 293

Yazdi MG, Ivanic M, Mohamed A, Uheida A (2018) Surface modified composite nanofibers for the removal of indigo carmine dye from polluted water. RSC Adv 8(43):24588 24598

Zhang M W, Lin K YA, Huang C F, Tong S (2019) Enhanced degrada tion of toxic azo dye, amaranth, in water using Oxone catalyzed by MIL 101 NH2 under visible light irradiation. Sep Purif Technol 227:115632

Zhong L, Li X, Liu R, Wei X, Li J (2019) A visible light driven photoelectrochemical molecularly imprinted sensor based on titani um dioxide nanotube arrays loaded with silver iodide nanoparticles for the sensitive detection of benzoyl peroxide. Analyst 144(10): 3405 3413